

Influence of Fc modifications and IgG subclass on biodistribution of humanized antibodies targeting L1CAM

Sai Kiran Sharma¹, Maya Suzuki^{2,3}, Hong Xu^{2,5}, Joshua A. Korsen^{1,6}, Zachary Samuels¹, Hongfen Guo^{2,5}, Brandon Nemieboka^{1,4}, Alessandra Piersigilli⁷, Kimberly J. Edwards¹, Nai-Kong V. Cheung^{*2,4,5}, Jason S. Lewis^{*,1,4,5,8,9}

¹ Department of Radiology, Memorial Sloan Kettering Cancer Center, New York, NY, USA

² Department of Pediatrics, Memorial Sloan Kettering Cancer Center, New York, NY, USA

³ Center for Clinical and Translational Research, Kyushu University Hospital, Fukuoka, Japan

⁴ Gerstner Sloan Kettering Graduate School of Biomedical Sciences, Memorial Sloan Kettering Cancer Center, New York, NY, USA

⁵ Molecular Pharmacology Program, Memorial Sloan Kettering Cancer Center, New York, NY, USA

⁶ Department of Pharmacology, Weill Cornell Medical College, New York, NY, USA

⁷ Tri-Institutional Laboratory of Comparative Pathology, Memorial Sloan Kettering Cancer Center, Weill Cornell Medical College, and The Rockefeller University, New York, NY, USA

⁸ Department of Radiology, Weill Cornell Medical College, New York, NY, USA

⁹ Radiochemistry and Molecular Imaging Probes Core, Memorial Sloan Kettering Cancer Center, New York, NY, USA

Running Title: Differential distribution of antibodies

Keywords: Immuno-PET; Aglycosylated antibody; Afucosylated antibody; Fab Arm Exchange

***Co-corresponding Authors:**

*Jason S. Lewis, Department of Radiology, Memorial Sloan Kettering Cancer Center, 1275 York Avenue, NY, 10065, USA; Email: lewisj2@mskcc.org Phone: (646) 888 3038

*Nai-Kong V. Cheung, Department of Pediatrics, Memorial Sloan Kettering Cancer Center, 1275 York Avenue, NY, 10065; Email: cheungn@mskcc.org Phone: (646) 888 2313

First Author:

Sai Kiran Sharma, Department of Radiology, Memorial Sloan Kettering Cancer Center, 1275 York Avenue, NY, 10065, USA; Email: saikiran@ualberta.ca Phone: (646) 832 9911

Word Count: 6328 (all inclusive)

Disclosure: NKC, MS, BN, HX and JSL were named as inventors on the LICAM patent (WO2018232188A1) filed by MSK. Both MSK and NKC have financial interest in Y-mAbs Therapeutics Inc., Abpro-Labs and Eureka Therapeutics. NKC reports receiving commercial research grants from Y-mAbs Therapeutics Inc., and Abpro-Labs Inc. NKC was named as inventor on multiple patents filed by MSK, including those licensed to Y-mAbs Therapeutics Inc., Biotech Pharmacon, and Abpro-labs. NKC is a SAB member for Abpro-Labs and Eureka Therapeutics. JSL is an Associate Editor of the Journal of Nuclear Medicine. JSL has no involvement or access to information regarding the peer-review of this article. SKS is a member of the editorial board of the Journal of Nuclear Medicine. No other potential conflicts of interest relevant to this article exist.

Financial Support: This work was supported by the MSKCC Small Animal Imaging Core - funded in part by the NIH Small-Animal Imaging Research Program (SAIRP) Grant R24 CA83084 and NIH Center Grant P30 CA08748, and the Tri-Institutional Laboratory of Comparative Pathology, which were funded in part by NIH grant P30 CA08748. The work was also supported by an R01 CA176671 awarded to JSL, and a diversity supplement R01 CA176671 awarded to (BN). BN was supported by a Medical Scientist Training Program grant from the National Institute of General Medical Sciences of the National Institutes of Health under award number T32GM007739 to the Weill Cornell/Rockefeller/Sloan Kettering Tri-Institutional MD-PhD Program. JSL was supported by R01 CA204167 and R35CA232130. JSL acknowledges funding support from the Mr. William H. Goodwin and Mrs. Alice Goodwin and the Commonwealth Foundation for Cancer Research and The Center for Experimental Therapeutics at Memorial Sloan Kettering Cancer Center. SKS acknowledges the Tow Foundation for Postdoctoral Fellowship Award.

ABSTRACT

Immuno-positron emission tomography (immuno-PET) is a powerful tool to noninvasively characterize the in vivo biodistribution of engineered antibodies (Abs). **Methods:** L1 cell adhesion molecule (L1CAM)-targeting HuE71 immunoglobulin G1 (IgG1) and immunoglobulin G4 (IgG4) Abs bearing identical variable heavy and light chain sequences but different fragment crystallizable (Fc) portions were radiolabeled with Zirconium-89 (^{89}Zr) and the in vivo biodistribution was studied in SKOV3 ovarian cancer xenografted nude mice. **Results:** In addition to showing uptake in L1CAM-expressing SKOV3 tumors like its parental counterpart HuE71 IgG1, the afucosylated variant having enhanced Fc-receptor (FcR) affinity showed high nonspecific uptake in lymph nodes. On the other hand, aglycosylated HuE71 IgG1 with abrogated FcR binding did not show lymphoid uptake. The use of IgG4 subclass showed high nonspecific uptake in the kidneys, which was prevented by mutating serine at position 228 to proline (S228P) in the hinge region of the IgG4 Ab to mitigate in vivo fragment antigen-binding (Fab) arm exchange. **Conclusion:** Our findings highlight the influence of Fc-modifications and the choice of IgG subclass on the in vivo biodistribution of Abs and the potential outcomes thereof.

INTRODUCTION

Monoclonal antibodies rank among the most sought after class of pharmaceuticals being developed for the treatment of several diseased conditions in humans (1). Their increasing utility has bolstered antibody (Ab) engineering efforts to improve efficacy and mitigate toxicities (2,3). Altering the glycosylation status, introducing point mutations in the fragment crystallizable (Fc) region, or changing the immunoglobulin G (IgG) subclass, are common strategies whereby the binding of an IgG to Fc gamma receptors (Fc γ R) on immune effector cells can be modulated (4-7). However, the impact of these modifications on Ab biodistribution has not been adequately examined. Arguably, most therapeutic Abs are unnaturally engineered biomolecules synthesized using recombinant technologies, hence their in vivo biodistribution cannot be taken for granted. Intriguingly, of all the FDA approved antibodies, only a few have dynamic time-dependent in vivo biodistribution and pharmacokinetics data profiled in patients (8). Furthermore, only a handful of these Abs have had preclinical biodistribution analysis before or after FDA approval (9). Longitudinal imaging by immuno-PET can fill this existing knowledge gap by enabling quantitation of the in vivo pharmacokinetics and biodistribution of Abs whilst delineating their on-target binding and off-target disposition. Critically, immuno-PET and biodistribution studies performed in relevant preclinical animal models early in Ab drug development campaigns can serve as a harbinger for clinical translation and success of Ab therapeutics in human patients. (10,11)

The majority of FDA-approved Ab therapeutics belong to the fully human or humanized IgG1 subclass. In addition to target-specific binding at the fragment antigen-binding (Fab) end of the the IgG molecule, human(ized) IgG1 Abs bind strongly to activating Fc γ Rs such as Fc γ RIIIa, which is expressed on immune effector cells such as natural killer cells to mediate antibody-dependent cellular cytotoxicity (ADCC) – a key mechanism of action of several therapeutic Abs. Furthermore, *afucosylated* IgG1 Abs lacking a core fucose in the N-linked

biantennary oligosaccharide units of the Fc region have stronger Fc-Fc γ RIIIa binding – leading to enhanced ADCC activity (Fig. 1) (12). On the other hand, *aglycosylated* IgG1 Abs lacking the N-linked biantennary oligosaccharide unit in the Fc region have abrogated Fc-Fc γ R interactions (Fig. 1) (13). Of late, IgG4 – the least abundant IgG in human serum has emerged as a subclass of choice for the development of therapeutic Abs including those used for immunotherapy (14). The low affinity of IgG4 Abs for activating Fc γ Rs but high affinity for the inhibitory Fc γ RIIB renders them relatively benign for ADCC. In fact, IgG4s are considered *anti-inflammatory* Abs owing to their ability to dampen immune responses against repetitive allergen exposure (15). These properties make IgG4 a subclass of choice for the design of immunotherapeutics such as nivolumab and pembrolizumab which bind to PD-1 on effector T cells in the tumor microenvironment and render efficacy without eliciting secondary immune mechanisms like ADCC (5,7,16). Collectively, all the aforementioned features highlight the importance of in vivo biomolecular interactions along the Fc-FcR axis that are worth considering during the design and development of therapeutic antibodies (17).

In the work at hand, we asked three questions fundamental to the molecular composition of humanized IgGs targeting the cell surface glycoprotein L1 cell adhesion molecule (L1CAM), without interfering with the Ab's ability to bind its cognate antigen or interact with the neonatal Fc receptor (FcRn). Foremost, we asked how enhancement of Fc-Fc γ R affinity by afucosylation impacts the in vivo distribution of humanized IgG1. Next, we were curious to know how Fc-silencing via Ab aglycosylation, which abrogates Fc-Fc γ R interaction influences the in vivo distribution of humanized IgG1. Lastly, we wanted to know how choice of IgG subclass – switching from IgG1 to IgG4 with and without fab arm exchange (FAE), and loss of most Fc functions affects Ab distribution in vivo. To that end, we developed a panel of humanized Abs (Fig. 1; Table 1) targeting human L1CAM, which is overexpressed in several malignancies (18,19). To noninvasively visualize the antibodies *in vivo*, we radiolabeled them with zirconium-

^{89}Zr) and utilized immuno-PET in athymic nude mice bearing subcutaneously implanted L1CAM-expressing SKOV3 tumors.

****FIGURE 1****

MATERIALS AND METHODS

Animal Model

All animals were treated as per guidelines approved by the Research Animal Resource Center and Institutional Animal Care and Use Committee at Memorial Sloan Kettering Cancer Center, NY. 8-10-week-old female athymic nude (Nu/Nu) mice were purchased from Charles River Laboratories. Animals were housed in ventilated cages, given food and water ad libitum, and allowed to acclimatize for 1 week prior to inoculation of tumor cells. SKOV3 tumors were induced on the right shoulder via subcutaneous injection of 5 million cells in a 150 μL cell suspension of 1:1 (v/v) mixture of fresh media/ Matrigel (BD Biosciences). The xenografted mice were used for in vivo studies when the tumor volumes reached $\sim 300 \text{ mm}^3$.

PET Imaging

PET imaging was conducted using a mouse hotel on an Inveon PET-CT scanner (Siemens Healthcare) (20). SKOV3 xenografted mice were intravenously administered ^{89}Zr -labeled antibodies (8 MBq; 45 μg suspended in 150 μL of PBS per mouse; $n=2$ mice per Ab variant). Animals were scanned under the influence of anesthesia by inhalation of 2% isoflurane (Baxter Healthcare) and medical air. PET data for each mouse was recorded via static scans at 48-, 96-, and 144-hours (h) post-injection (p.i.). The PET-CT images were calibrated and cropped prior to analysis and scaled using AMIDE software (Stanford University). The images were rendered using VivoQuant (Invicro).

Biodistribution

Ex vivo biodistribution analysis was performed in a separate cohort of SKOV3 xenografted mice that were intravenously administered 1.15 MBq; 6.4 µg of each ⁸⁹Zr-labeled Ab variant suspended in 150 µL of PBS per mouse. An n=6 animals were used per Ab variant wherein 3 animals were injected with ⁸⁹Zr-labeled Ab alone and 3 animals were injected with a mixture of ⁸⁹Zr-labeled Ab and 38-fold excess (mass) of the unlabeled Ab variant. Animals were euthanized by CO₂ asphyxiation at 144 h (p.i.). Following euthanasia, tissues of interest were harvested via necropsy, weighed, and assayed for radioactivity on a gamma counter calibrated for Zr-89. Counts were converted into activity using a calibration curve generated from known standards. Count data were background and decay corrected to the time of injection, and the percent injected dose per gram (%ID/g) for each tissue sample was calculated by normalization to the total activity injected.

Statistics

All data are expressed as mean ± standard deviation (SD). Statistical analysis was performed using GraphPad Prism version 9.1.0. Statistical comparisons of radioactivity concentrations in each organ across the various groups in the *ex vivo* biodistribution studies were done using non-parametric multiple Mann-Whitney tests to compare ranks. The Holm-Sidak multiple comparison test was applied, and the threshold for p value comparison was set to 0.05.

RESULTS

A panel of IgG1 and IgG4 antibodies having identical variable heavy and light chain sequences targeting human L1CAM but modified Fc regions was generated (Table 1) to gain insights into the influence of Fc-modifications and subclass on the in vivo biodistribution of IgG1 and IgG4 Abs respectively.

****TABLE 1****

Following purification of the various ^{89}Zr -labeled antibodies, we obtained radioimmunoconjugates having an average molar activity of 26.6 MBq/nmol. Cell-based immunoreactivity assay confirmed the ability of the various radioimmunoconjugates to bind L1CAM-expressing SKOV3 cells (21) (Table 1; Supplemental Fig. 1). Incubation of the radioimmunoconjugates in serum and evaluation by radio-instant thin layer chromatography demonstrated less than 4% demetallation up to 7 days after radiosynthesis – suggesting high stability of the radioimmunoconjugates in a biologically-relevant medium (Supplemental Fig. 2). Size exclusion high performance liquid chromatography of the ^{89}Zr -labeled antibodies incubated without a radioprotectant in chelexed phosphate-buffered saline at 37 °C showed more than 80% of the radioimmunoconjugates being stable and existing as monomers up to 6 days post-radiosynthesis (Supplemental Figs. 3 and 4).

Athymic nude mice were used in our studies owing to their ability to grow tumors from implanted human cancer cell lines and the presence of functional innate immune cells such as macrophages, dendritic cells and natural killer (NK) cells in this strain. Macrophages and NK cells comprise two main Fc-dependent effector cells responsible for eliciting antibody-dependent cellular phagocytosis (ADCP) and cytotoxicity (ADCC) respectively (22). Furthermore, despite only 60-70% homology between mouse and human Fc γ Rs, human IgGs are reported to bind orthologous mouse Fc γ Rs with similar strength – suggestive of potentially similar downstream biological activities mediated by hFc-mFc γ R interactions in mice (23). Immuno-PET imaging of

the three ⁸⁹Zr-labeled IgG1 variants – HuE71-IgG1, HuE71-IgG1-Afuco, and HuE71-IgG1-Aglyco demonstrated uptake of radioactivity in SKOV3 tumors (Fig. 2A-C). However, the three IgG1 variants yielded distinct vivo distribution patterns of radioactivity. SKOV3 xenografted mice injected with ⁸⁹Zr-HuE71-IgG1 showed persistence of radioactivity in blood up to 96 h p.i. – suggesting slow in vivo clearance of L1CAM-targeted Abs in this model (Fig. 2A). Besides target-specific tumoral uptake of radioactivity, non-specific uptake was found in the liver and joints of the long bones of mice. Similarly, ⁸⁹Zr- HuE71-IgG1-Afuco yielded uptake of radioactivity in the tumor, liver and joints of the long bones. However, this variant revealed high intensity bilateral hotspots corresponding to the axillary and cervical lymph nodes (Fig. 2B) and demonstrated faster clearance from circulation relative to ⁸⁹Zr- HuE71-IgG1. Additionally, ⁸⁹Zr-HuE71-IgG1-Afuco outlined the spleen and showed higher radioactivity concentration in long bone joints and the vertebral column. The faster clearance and elevated non-specific tissue uptake patterns observed for ⁸⁹Zr-HuE71-IgG1-Afuco may be attributed to enhanced binding of the afucosylated Fc with mouse FcγRIV-expressing immune cells in the lymph nodes and reticuloendothelial system (RES). The latter is exemplified by results from the analysis of Fc-FcγR binding by surface plasmon resonance (SPR) (Table 2). Notably, conjugation of desferrioxamine (DFO) to lysine residues distributed randomly in the Fc region of IgG1 molecules did not impact binding to mFcRIV and hFcRIIIa-158V.

****TABLE 2****

Previous studies found significant increases in the binding affinity of afucosylated IgG1 Ab to human FcγRIIIa (hFcγRIIIa) but no change in the binding affinity to hFcγRI and hFcRn (12,24,25). So, we focused our SPR analysis of the differentially glycosylated IgG1 Fc-variants to hFcγRIIIa. Murine FcγRIV (mFcγRIV) was included in the SPR assay since it is a functional ortholog of hFcγRIIIa, and binding to mFcγRIV may contextualize findings from in vivo studies carried out in mice (26). Notably, ADCC in humans is mediated via interaction of the Fc of

target antigen-bound hIgG1 and hFc γ RIIIa expressed on immune effector cells. Furthermore, afucosylated human(ized) IgG1 Abs have been shown to target mFc γ RIV for enhanced tumor therapy by ADCC in mice (27). SPR analysis of the anti-L1CAM IgG1 variants used in our study demonstrated 3-fold higher affinity of the HuE71-IgG1-Afuco for mFc γ RIV compared to HuE71-IgG1. Interestingly, HuE71-IgG1-Afuco also showed a similar 3-fold higher binding to the 158V isoform of human Fc γ RIIIa. On the other hand, and as expected, HuE71-IgG1-Afuco showed no binding to either mouse or human Fc γ Rs. Lastly, immuno-PET of ^{89}Zr -HuE71-IgG1-Aglyco in SKOV3 xenografted mice displayed tumoral uptake of radioactivity with relatively lower concentration in the liver and bone joints and no detectable uptake in lymph nodes (Fig. 2C). ^{89}Zr -HuE71-IgG1-Aglyco demonstrated the longest persistence of radioactivity in systemic circulation – suggesting enhanced in vivo half-life plausibly due to the lack of hFc-mFc γ RIV interactions with resident immune effector cells in the lymph nodes and RES.

******FIGURE 2******

Quantification of the in vivo biodistribution of the three L1CAM-targeted IgG1 variants was done in a separate cohort of SKOV3 xenografts injected with the ^{89}Zr -labeled anti-L1CAM-targeted Fc-modified Abs. Foremost, the three IgG1 variants displayed differential radioactivity concentrations in the blood. ^{89}Zr -HuE71-IgG1-Afuco showed <1% ID/g remaining in circulation at 144 h p.i. whereas the other two variants showed up to 6% ID/g at this timepoint. Next, ^{89}Zr -HuE71-IgG1-Afuco demonstrated high liver uptake (10.8 ± 2.1 %ID/g) compared to the other two variants which showed less than 6% ID/g in this tissue. Most other non-target tissues showed unremarkable differences in uptake of radioactivity between the three Fc-modified IgG1 variants. However, axillary lymph nodes isolated from SKOV3 xenografted mice injected with ^{89}Zr -HuE71-IgG1-Aglyco yielded significantly lesser radioactivity concentration in this tissue. Unlike PET images, only mice injected with ^{89}Zr -HuE71-IgG1 demonstrated significantly higher radioactivity concentration in the bone (femur) compared to xenografts injected with ^{89}Zr -

HuE71-IgG1-Aglyco. Indeed, SKOV3 tumors showed high and specific uptake of radioactivity for all three ^{89}Zr -labeled L1CAM-targeted IgG1 variants. However, the tumoral uptake values (%ID/g) in mice dosed with the unblocked L1CAM-targeted ^{89}Zr -radioimmunoconjugates demonstrated significantly lower uptake of ^{89}Zr -HuE71-IgG1-Afuco compared to radioimmunoconjugates of the other two IgG1 variants. The relatively low tumoral uptake (7.7 ± 2 %ID/g) of ^{89}Zr -HuE71-IgG1-Afuco may be attributed to a significant proportion of the radioactivity/antibody being concentrated in the liver and lymph nodes of SKOV3 xenografted mice. Determining the percentage of total injected dose of radioactivity (%ID) taken up in the various tissues revealed that despite having the highest radioactivity concentration (%ID/g) for ^{89}Zr -HuE71-IgG1-Afuco, there was less than 2% of the total injected radioactivity in the axillary lymph nodes at 144 h p.i. Instead, the liver accumulated more radioactivity (17.6 ± 3.4 %ID) and turned out to be a major sink for the afucosylated IgG1 variant.

Importantly, the histopathologic examination of lymph nodes harvested from SKOV3 xenografted mice injected with ^{89}Zr -HuE71-IgG1-Afuco showed no morphologic evidence of infiltrating neoplastic cells. Instead, these nodes demonstrated reactive hyperplasia characterized by marked paracortical and medullary histio- and plasmacytosis (Fig. 2E). The latter was a unique feature relative to lymph nodes harvested from SKOV3 xenografted mice and tumor-naïve mice that never received ^{89}Zr -HuE71-IgG1-Afuco. Along those lines, axillary lymph nodes harvested from SKOV3 xenografted mice injected with ^{89}Zr -HuE71-IgG1 and ^{89}Zr -HuE71-IgG1-Aglyco showed minor sinus histiocytosis but displayed normal lymphoid tissue architecture (Fig. 2E).

Next, we studied the influence of IgG subclass on the in vivo biodistribution of Ab drugs. To delineate the in vivo biodistribution of IgG4 Abs, we generated a humanized IgG4 variant of the L1CAM-targeting Ab and conducted serial PET imaging studies in SKOV3 xenografted mice. Serial PET imaging of ^{89}Zr -HuE71-IgG4 revealed slow in vivo clearance of the Ab from

blood and high radioactivity concentration in the liver (Fig. 3A). In addition to tumoral uptake of radioactivity, ^{89}Zr -HuE71-IgG4 showed radioactivity concentration in the kidneys and axillary lymph nodes of SKOV3 xenografts. We hypothesized that uptake of radioactivity in the kidneys may be attributed to Fab arm exchange (FAE), leading to instability of the Ab *in vivo*. FAE is an intrinsic property of the IgG4 subclass whereby two half-molecules (heavy-light chain pair) of the Abs dissociate from one another at the hinge and recombine spontaneously with other IgG4 half-molecules in serum to form monovalent bispecific antibodies *in vitro* and *in vivo* (28). Introducing a point mutation from serine to proline at position 228 (S228P) in the hinge region of IgG4 antibodies has been shown to mitigate the propensity of FAE (6). To validate our hypothesis, an S228P hinge-mutated IgG4 variant – ^{89}Zr -HuE71-IgG4M – was synthesized and evaluated *in vivo*. ^{89}Zr -HuE71-IgG4M demonstrated gradual accretion of radioactivity in the SKOV3 tumor whilst showing little to no radioactivity in the kidneys (Fig. 3B). Of note, ^{89}Zr -HuE71-IgG4M faintly highlighted the liver, axillary lymph nodes and bone joints in this model.

****FIGURE 3****

The use of an IgG4 variant of the anti-GD2 Ab, Hu3F8 as an isotype control and the similarity in radioactivity uptake in the kidneys of SKOV3 xenografted mice injected with ^{89}Zr -Hu3F8-IgG4 and ^{89}Zr -HuE71-IgG4 further validated that the abnormal kidney uptake is attributed to FAE intrinsic to IgG4 Abs (Fig. 3C). Further, results from *ex vivo* biodistribution analysis performed in SKOV3 xenografted mice injected with the three ^{89}Zr -labeled IgG4 antibodies corroborated findings from immuno-PET studies (Fig. 3D). Importantly, ^{89}Zr -HuE71-IgG4M yielded significantly lower radioactivity concentration (2.5 ± 0.56 %ID/g) in the kidneys compared to ^{89}Zr -HuE71-IgG4 (7.4 ± 2.32 %ID/g; $p=0.02$). Furthermore, blockade of tumoral uptake of radioactivity by co-injection of 0.25 mg/kg of ^{89}Zr -labeled IgG4 Ab with 38-fold excess (mass) of unmodified L1CAM-targeted IgG4 Abs in *ex vivo* biodistribution studies confirmed target-mediated uptake in SKOV3 tumors (Fig. 3D). Notably, ^{89}Zr -HuE71-IgG4M

demonstrated higher tumoral uptake of radioactivity (16.1 ± 4.26 %ID/g) compared to ^{89}Zr -HuE71-IgG4 (5.5 ± 2.4 %ID/g; $p=0.03$) and ^{89}Zr -Hu3F8-IgG4 (3.6 ± 1.76 %ID/g; $p=0.02$). Concordant with PET data, ^{89}Zr -Hu3F8-IgG4 yielded high radioactivity concentration in the kidneys (15.2 ± 5.14 %ID/g) and showed between 1-8 % ID/g in most healthy tissues. Tumoral uptake (4.9 ± 0.46 %ID/g) of the isotype Ab may be attributed to enhanced permeability and retention in this compartment. Lastly, the high radioactivity concentration in multiple tissues harvested from mice injected with the ^{89}Zr -HuE71-IgG4M-blocking dose arm is most likely a result of persistence of ^{89}Zr -HuE71-IgG4M in the blood at 144 h p.i.

DISCUSSION

Recent insights into pharmacologic modulation at the Fc-Fc γ R axis have made this molecular interaction an important consideration in the development of Ab-based drugs for cancer immunotherapy (16,17,29). Furthermore, single nucleotide polymorphisms in Fc γ R-encoding genes have been implicated in disease etiology and clinical responses (30). Specifically, patients carrying the 158V/V genotype showed improved outcomes from rituximab therapy, due, in part, to improved ADCC activity in vivo (31). Additionally, we have previously shown that stronger in vitro Fc-Fc γ R binding for an afucosylated (Afuco) variant of the humanized anti-GD2 IgG1 Ab yielded improved preclinical efficacy owing to enhanced ADCC in vivo (25).

Our current findings with the afucosylated anti-L1CAM IgG1 variant concur broadly with two ^{89}Zr -immuno-PET studies done using HER3-targeted humanized IgG1 Abs – GSK2849330 and RG7116, which were Fc-glycoengineered for enhanced ADCC activity (32,33). The high uptake of radioactivity in the liver and spleen of xenograft models developed in immunodeficient SCID mice used in those studies was attributed to enhanced binding of the Abs with Fc γ Rs expressed on tissue resident auxiliary immune cells in the RES (32,33). However, neither of those Abs showed elevated radioactivity concentrations in lymph nodes. The

latter may be due, in part, to the higher immunodeficient status of SCID mice used in those studies and the presence of functional NK cells in athymic nude mice used in our study. Although suggestive of an Fc-mediated phenomenon, the pronounced lymph node uptake of radioactivity in mice injected with the Afuco variant warrants further validation in immunocompetent syngeneic tumor models or xenograft models developed in mice reconstituted with a functional human immune system. Admittedly, immunodeficient mice impact the in vivo biodistribution of exogenously injected human(ized) IgG1 due to relatively low titers of endogenous IgG and the availability of unoccupied high affinity Fc γ R3 on tissue-resident immune cells in the liver, spleen and bone marrow (34). This phenomenon is exacerbated in highly immunodeficient mouse strains developed on the NOD-SCID background (35). However, low levels of serum IgG2a in athymic nude mice have also been implicated in the rapid clearance of exogenously injected human IgG1 and mouse IgG2a (36).

Along those lines, a comparison of the Afuco vs. parental L1CAM-targeting IgG1 in tumor naïve athymic nude mice revealed lower radioactivity concentration of ⁸⁹Zr-HuE71-IgG1-Afuco in the blood at 120 h p.i. – suggesting faster in vivo pharmacokinetics (Supplemental Fig. 5), which is consistent with our findings for this variant in SKOV3 xenografted mice. Furthermore, the relatively high radioactivity concentration in the long bone joints of mice injected with ⁸⁹Zr-HuE71-IgG1-Afuco is also indicative of faster in vivo catabolism of the radioimmunoconjugate, leading to the release of Zr-89 for in vivo uptake and complexation with hydroxyapatite in the bone joints. When target expression is absent in the bones, radioactivity uptake in this tissue is commonly attributed to the in vivo catabolism of DFO-conjugated ⁸⁹Zr-labeled antibodies in mice and the osteophilic nature of Zr-89 (37). Intriguingly, there was no significant difference between radioactivity concentrations in the liver or the axillary lymph nodes harvested from tumor-naïve mice injected with either ⁸⁹Zr-labeled L1CAM-targeted IgG1 variant. The latter points to a potential contribution of the tumor – a target sink, which may

account for a pronounced difference noted between ^{89}Zr -HuE71-IgG1 versus ^{89}Zr -HuE71-IgG1-Afuco in SKOV3 xenografted animals. Taken together, our findings suggest that afucosylated IgG1 antibodies having improved Fc-Fc γ R binding and enhanced ADCC capability are likely to have significantly faster in vivo pharmacokinetics due to sequestration in the RES and resident immune cells in lymph nodes. On the other hand, IgG1 aglycosylation yielded an Fc-silenced antibody, which showed no lymph node uptake when tested in the same animal model as its Fc-active counterparts.

In light of our findings with the L1CAM-targeting IgG4 variants, it is no surprise that several FDA-approved IgG4 Ab therapeutics harbor the S228P mutation to impart in vivo stability whilst minimizing therapeutic variability due to in vivo FAE (14). Of interest, lower uptake of radioactivity was found in the bone joints of SKOV3 xenografted mice injected with L1CAM-targeted ^{89}Zr -labeled IgG4 antibodies compared to their Fc-active IgG1 counterparts. Case in point, femurs harvested from SKOV3 xenografted mice injected with ^{89}Zr -HuE71-IgG4 and ^{89}Zr -HuE71-IgG4M showed 4.0 ± 0.74 %ID/g; $p=0.03$, and 4.4 ± 1.58 %ID/g; $p=0.047$ respectively compared to ^{89}Zr -HuE71-IgG1 which yielded 8.3 ± 2.35 %ID/g in this tissue. Furthermore, radioactivity concentrations of ^{89}Zr -labeled L1CAM-targeted IgG4 variants were comparable to that yielded by the Fc-silent IgG1 variant – ^{89}Zr -HuE71-IgG1-Aglyco (3.7 ± 0.75 %ID/g) in this tissue. The latter is suggestive of slow in vivo catabolism and low non-specific uptake in healthy non-target tissue(s). Lastly, the non-specific hepatic uptake of radioactivity highlights a plausible contribution of Fc-Fc γ R interactions between Fc-active radiolabeled IgG1s and parenchymal as well as non-parenchymal cells in the liver (38). It is known that the liver is involved in the in vivo catabolism of radiometal-labeled antibodies, leading to initial accumulation of ^{89}Zr -radiometabolites and subsequent complexation of free Zr-89 in the long bone joints of mice (37,39,40).

Highlights aside, a limitation of the current work is that it utilizes Ab variants developed

for a single tumor-associated antigen in a singular xenograft model developed on an immunodeficient background. Additionally, identification of cells having elevated expression of mFc γ RIV in lymph nodes leading to the manifestation of reactive hyperplasia, or pinpointing cells in the liver that bind ADCC-enhanced IgG1 antibodies to impact in vivo pharmacokinetics are outstanding questions that warrant further investigation.

CONCLUSION

Collectively, our findings highlight the influence of Fc-glycosylation status and choice of IgG subclass on the in vivo biodistribution of the most widely used human(ized) Ab subclasses (IgG1 and IgG4) approved as therapeutics for human use. Our results demonstrate that deglycosylated IgG1 Abs yield low non-specific off-target uptake in healthy tissues, whereas S228P hinge-mutated IgG4 Ab eliminates FAE-mediated renal uptake of radioactivity. Importantly, this work illustrates the value of immuno-PET to delineate the in vivo biodistribution of ADCC-enhanced IgG1 Abs and to macroscopically highlight potential non-tumor tissue depots. Doing so can inform Ab drug development efforts to uncover mechanisms leading to in vivo therapeutic benefit or toxicity. From a theranostic perspective, our results suggest that developing immuno-PET agents using ADCC-enhanced tumor-targeting IgG1 Abs may yield false-positive results in lymph nodes owing to Fc-Fc γ R interactions in vivo. Similarly, immuno-PET agents developed using tumor-targeting wildtype IgG4 Abs may yield false-positive results from non-specific uptake of radioactivity in the kidneys whilst grossly underestimating tumor burden due to loss of the radiotracer to in vivo FAE. In sum, we hope that the results described herein further motivate the utilization of molecular imaging to inform the preclinical development of novel Ab-based theranostic agents.

KEY POINTS

QUESTION: What is the impact of Fc-modification and choice of IgG subclass on the in vivo pharmacologic profile of humanized anti-tumor antibodies?

PERTINENT FINDINGS: Humanized IgG1 antibodies yield differential in vivo pharmacokinetics and biodistribution based on the glycosylation status of the Fc. Afucosylated IgG1 antibodies with enhanced Fc-Fc γ R binding and ADCC activity yield faster in vivo pharmacokinetics and show non-specific Fc-mediated sequestration in lymph nodes and reticuloendothelial system. Aglycosylated IgG1 antibodies with abrogated Fc-Fc γ R binding yield lesser non-specific uptake of the antibody and related radiocatabolites in vivo – yielding stealth targeting vectors. S228P hinge mutated IgG4 antibodies overcome in vivo fab arm exchange to yield a better radiopharmacologic profile by eliminating uptake of antibody and associated radioactivity in the kidneys.

IMPLICATIONS FOR PATIENT CARE: Using immuno-PET to characterize the in vivo pharmacokinetics and biodistribution to uncover potential mechanism of action or toxicity of engineered antibodies can yield better and safe antibody-based drugs to improve patient care.

REFERENCES

1. Carter PJ, Lazar GA. Next generation antibody drugs: pursuit of the 'high-hanging fruit'. *Nat Rev Drug Discov.* 2018;17:197-223.
2. Weiner GJ. Building better monoclonal antibody-based therapeutics. *Nat Rev Cancer.* 2015;15:361-370.
3. Wang X, Mathieu M, Brezski RJ. IgG Fc engineering to modulate antibody effector functions. *Protein Cell.* 2018;9:63-73.
4. Arnold JN, Wormald MR, Sim RB, Rudd PM, Dwek RA. The impact of glycosylation on the biological function and structure of human immunoglobulins. *Annu Rev Immunol.* 2007;25:21-50.
5. Bruhns P, Iannascoli B, England P, et al. Specificity and affinity of human Fcγ receptors and their polymorphic variants for human IgG subclasses. *Blood.* 2009;113:3716-3725.
6. Silva JP, Vetterlein O, Jose J, Peters S, Kirby H. The S228P mutation prevents in vivo and in vitro IgG4 Fab-arm exchange as demonstrated using a combination of novel quantitative immunoassays and physiological matrix preparation. *J Biol Chem.* 2015;290:5462-5469.
7. Vidarsson G, Dekkers G, Rispens T. IgG subclasses and allotypes: from structure to effector functions. *Front Immunol.* 2014;5:520.
8. O'Donoghue JA, Lewis JS, Pandit-Taskar N, et al. Pharmacokinetics, biodistribution, and radiation dosimetry for (89)Zr-Trastuzumab in patients with esophagogastric cancer. *J Nucl Med.* 2018;59:161-166.
9. Ulaner GA, Sobol NB, O'Donoghue JA, et al. CD38-targeted immuno-PET of multiple myeloma: from xenograft models to first-in-human imaging. *Radiology.* 2020;295:606-615.
10. Crawford A, Haber L, Kelly MP, et al. A Mucin 16 bispecific T cell-engaging antibody for the treatment of ovarian cancer. *Sci Transl Med.* 2019;11:497:eaau7534.
11. Kelly MP, Makonnen S, Hickey C, et al. Preclinical PET imaging with the novel human antibody (89)Zr-DFO-REGN3504 sensitively detects PD-L1 expression in tumors and normal tissues. *J Immunother Cancer.* 2021;9:1:e002025.
12. Shields RL, Lai J, Keck R, et al. Lack of fucose on human IgG1 N-linked oligosaccharide improves binding to human Fcγ RIII and antibody-dependent cellular toxicity. *J Biol Chem.* 2002;277:26733-26740.
13. Radaev S, Sun PD. Recognition of IgG by Fcγ receptor. The role of Fc glycosylation and the binding of peptide inhibitors. *J Biol Chem.* 2001;276:16478-16483.
14. Chen X, Song X, Li K, Zhang T. Fcγ R-binding is an important functional attribute for immune checkpoint antibodies in cancer immunotherapy. *Front Immunol.* 2019;10:292.
15. Davies AM, Sutton BJ. Human IgG4: a structural perspective. *Immunol Rev.* 2015;268:139-159.
16. Dahan R, Segal E, Engelhardt J, Selby M, Korman AJ, Ravetch JV. Fcγ R modulate the anti-tumor activity of antibodies targeting the PD-1/PD-L1 axis. *Cancer Cell.* 2015;28:285-295.

17. DiLillo DJ, Ravetch JV. Fc-Receptor interactions regulate both cytotoxic and immunomodulatory therapeutic antibody effector functions. *Cancer Immunol Res.* 2015;3:704-713.
18. Schafer MK, Altevogt P. L1CAM malfunction in the nervous system and human carcinomas. *Cell Mol Life Sci.* 2010;67:2425-2437.
19. Ganesh K, Basnet H, Kaygusuz Y, et al. L1CAM defines the regenerative origin of metastasis-initiating cells in colorectal cancer. *Nat Cancer.* 2020;1:28-45.
20. Carter LM, Henry KE, Platzman A, Lewis JS. 3D-printable platform for high-throughput small-animal imaging. *J Nucl Med.* 2020;61:1691-1692.
21. Lindmo T, Boven E, Cuttitta F, Fedorko J, Bunn PA, Jr. Determination of the immunoreactive fraction of radiolabeled monoclonal antibodies by linear extrapolation to binding at infinite antigen excess. *J Immunol Methods.* 1984;72:77-89.
22. Budzynski W, Radzikowski C. Cytotoxic cells in immunodeficient athymic mice. *Immunopharmacol Immunotoxicol.* 1994;16:319-346.
23. Overdijk MB, Verploegen S, Ortiz Buijsse A, et al. Crosstalk between human IgG isotypes and murine effector cells. *J Immunol.* 2012;189:3430-3438.
24. Junttila TT, Parsons K, Olsson C, et al. Superior in vivo efficacy of afucosylated trastuzumab in the treatment of HER2-amplified breast cancer. *Cancer Res.* 2010;70:4481-4489.
25. Xu H, Guo H, Cheung IY, Cheung NK. Antitumor efficacy of anti-GD2 IgG1 is enhanced by Fc glyco-engineering. *Cancer Immunol Res.* 2016;4:631-638.
26. Bruhns P. Properties of mouse and human IgG receptors and their contribution to disease models. *Blood.* 2012;119:5640-5649.
27. Braster R, Bogels M, Benonisson H, et al. Afucosylated IgG targets FcγR4 for enhanced tumor therapy in mice. *Cancers (Basel).* 2021;13(10):2372.
28. Rispens T, Ooijevaar-de Heer P, Bende O, Aalberse RC. Mechanism of immunoglobulin G4 Fab-arm exchange. *J Am Chem Soc.* 2011;133:10302-10311.
29. Arlauckas SP, Garris CS, Kohler RH, et al. In vivo imaging reveals a tumor-associated macrophage-mediated resistance pathway in anti-PD-1 therapy. *Sci Transl Med.* 2017;9:389:eaal3604.
30. Paul P, Pedini P, Lyonnet L, et al. FCGR3A and FCGR2A genotypes differentially impact allograft rejection and patients' survival after lung transplant. *Front Immunol.* 2019;10:1208.
31. Mellor JD, Brown MP, Irving HR, Zalberg JR, Dobrovic A. A critical review of the role of Fcγ receptor polymorphisms in the response to monoclonal antibodies in cancer. *J Hematol Oncol.* 2013;6:1.
32. Alsaïd H, Skedzielewski T, Rambo MV, et al. Non invasive imaging assessment of the biodistribution of GSK2849330, an ADCC and CDC optimized anti HER3 mAb, and its role in tumor macrophage recruitment in human tumor-bearing mice. *PLoS One.* 2017;12:e0176075.
33. Terwisscha van Scheltinga AG, Lub-de Hooge MN, Abiraj K, et al. ImmunoPET and biodistribution with human epidermal growth factor receptor 3 targeting antibody 89Zr-RG7116. *MAbs.* 2014;6:1051-1058.

34. Sharma SK, Chow A, Monette S, et al. Fc-mediated anomalous biodistribution of therapeutic antibodies in immunodeficient mouse models. *Cancer Res.* 2018;78:1820-1832.
35. Li F, Ulrich ML, Shih VF, et al. Mouse strains influence clearance and efficacy of antibody and antibody-drug conjugate via Fc-FcγR interaction. *Mol Cancer Ther.* 2019;18:780-787.
36. Reddy N, Ong GL, Behr TM, Sharkey RM, Goldenberg DM, Mattes MJ. Rapid blood clearance of mouse IgG2a and human IgG1 in many nude and nu/+ mouse strains is due to low IgG2a serum concentrations. *Cancer Immunol Immunother.* 1998;46:25-33.
37. Chomet M, Schreurs M, Bolijn MJ, et al. Head-to-head comparison of DFO* and DFO chelators: selection of the best candidate for clinical (89)Zr-immuno-PET. *Eur J Nucl Med Mol Imaging.* 2021;48:3:694-707.
38. Jones PL, Brown BA, Sands H. Uptake and metabolism of 111In-labeled monoclonal antibody B6.2 by the rat liver. *Cancer Res.* 1990;50:852s-856s.
39. Meijs WE, Haisma HJ, Klok RP, et al. Zirconium-labeled monoclonal antibodies and their distribution in tumor-bearing nude mice. *J Nucl Med.* 1997;38:112-118.
40. Motta-Hennessy C, Sharkey RM, Goldenberg DM. Metabolism of indium-111-labeled murine monoclonal antibody in tumor and normal tissue of the athymic mouse. *J Nucl Med.* 1990;31:1510-1519.

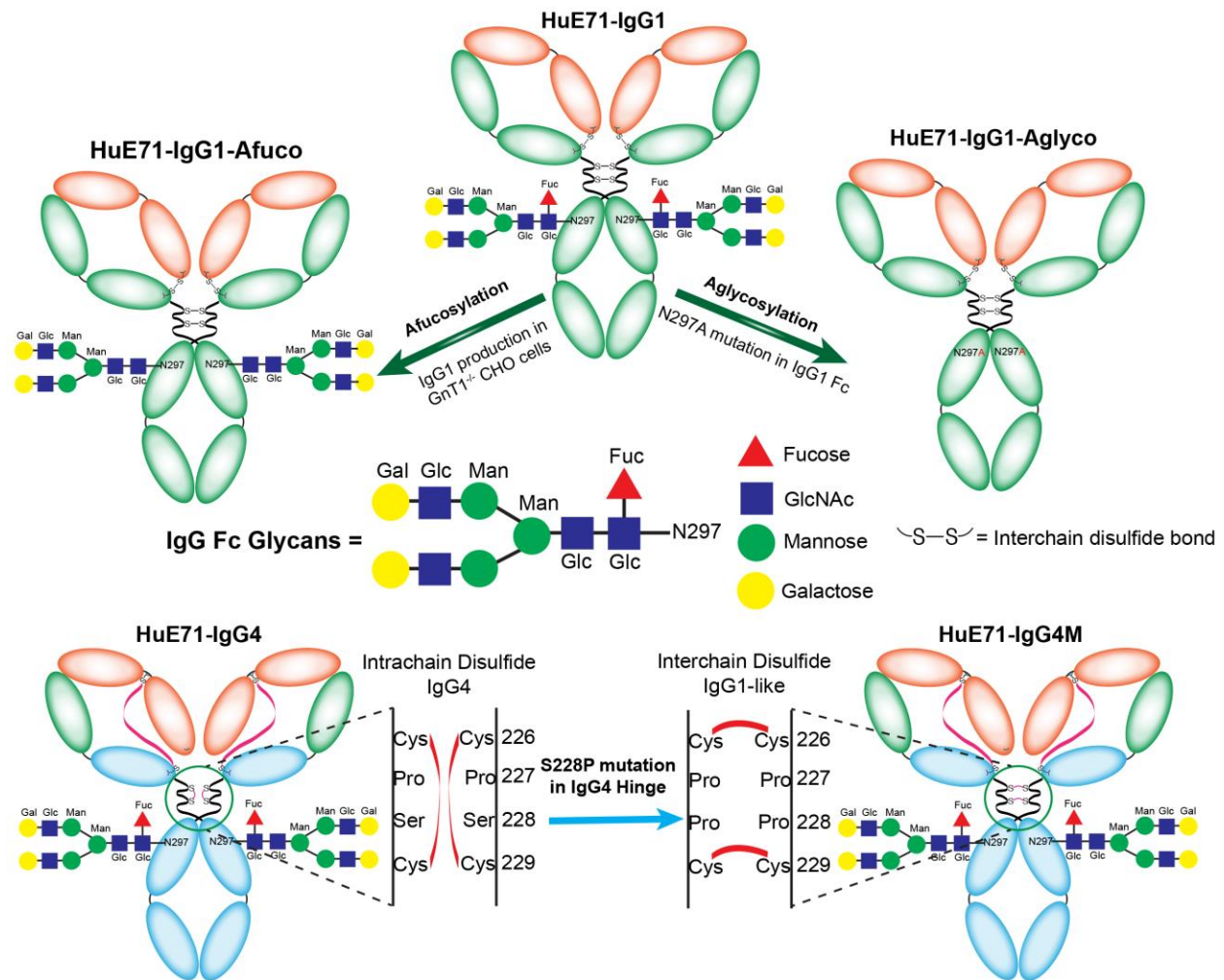


FIGURE 1 Schematic describing the generation of Fc-variants of humanized IgG1 and hinge mutated IgG4 L1CAM-targeted antibodies: Fc-glycosylated variants of an L1CAM-targeted humanized IgG1 Ab, HuE71-IgG1 (top center) were obtained by producing the IgG1 Ab in $GnT1^{-/-}$ CHO cells that are defective for fucosylation and thus yield HuE71-IgG1-Afuco (top left) (25); whereas substituting asparagine at position 297 in the Fc region to alanine (N297A) yielded an aglycosylated variant, HuE71-IgG1-Aglyco (top right). Engrafting anti-L1CAM binding variable heavy and variable light chain sequences onto the IgG4 framework yielded HuE71-IgG4 (bottom left). Mutating serine at position 228 to proline (S228P) in the hinge region of HuE71-IgG4 yielded HuE71-IgG4M. (Fuc = Fucose; Glc = N-acetylglucosamine; Man = Mannose; Gal = N-acetylgalactosamine).

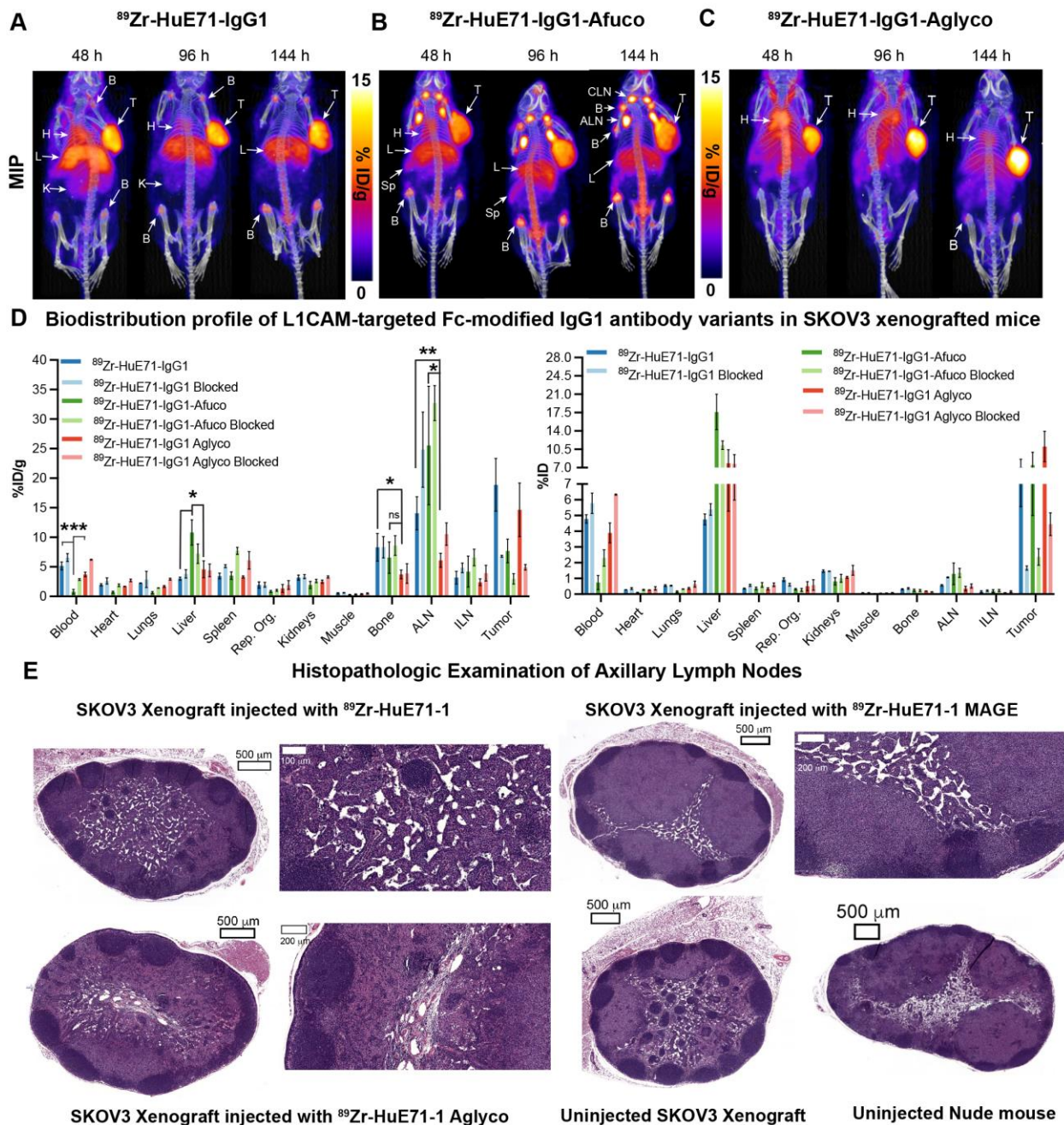


FIGURE 2. Immuno-PET imaging, ex vivo biodistribution analysis and histopathology delineate the differential in vivo profiles of Fc-modified L1CAM-targeted IgG1 variants in SKOV3 xenografted mice. Longitudinal PET-CT images acquired at 48, 96 and 144 h p.i. of 1.8 mg/kg; 7.95 MBq; 45 μg of (A) ^{89}Zr -HuE71-IgG1; (B) ^{89}Zr -HuE71-IgG1-Afuco; and (C) ^{89}Zr -HuE71-IgG1-Aglyco showing distribution of radioactivity in the blood (indicated by the heart; H), tumor (T), liver (L), long bone joints, axillary (ALN), cervical lymph nodes (CLN), spleen (Sp); Maximum intensity projections (MIPs) were calibrated and scaled 0-15% ID/g. (D) Ex vivo biodistribution profile (%ID/g vs. %ID) at

144 h p.i. of 0.25 mg/kg (1.15 MBq; 6.4 μ g) of the three ^{89}Zr -labeled L1CAM-targeted Fc-modified IgG1 variants and their corresponding low specific activity blocking dose groups in SKOV3 xenografted mice. On the graphs, ILN = Inguinal Lymph Node; * represents p value ≤ 0.03 ; ** represents p value ≤ 0.01 ; *** represents p value ≤ 0.0005 ; Detailed % ID/g and %ID values can be found in [Supplemental Tables 1 and 2](#). (E) A panel of representative low and high magnification H&E images from histopathologic examination of axillary lymph nodes harvested from SKOV3 xenografted mice injected with the three ^{89}Zr -labeled L1CAM-targeted IgG1 Fc-variants compared to low magnification images of axillary lymph nodes harvested from an un-injected SKOV3 xenografted mouse and a healthy tumor-naïve nude mouse. Scale bars on low magnification images represent 500 μm whereas high magnification images represent 200 μm .

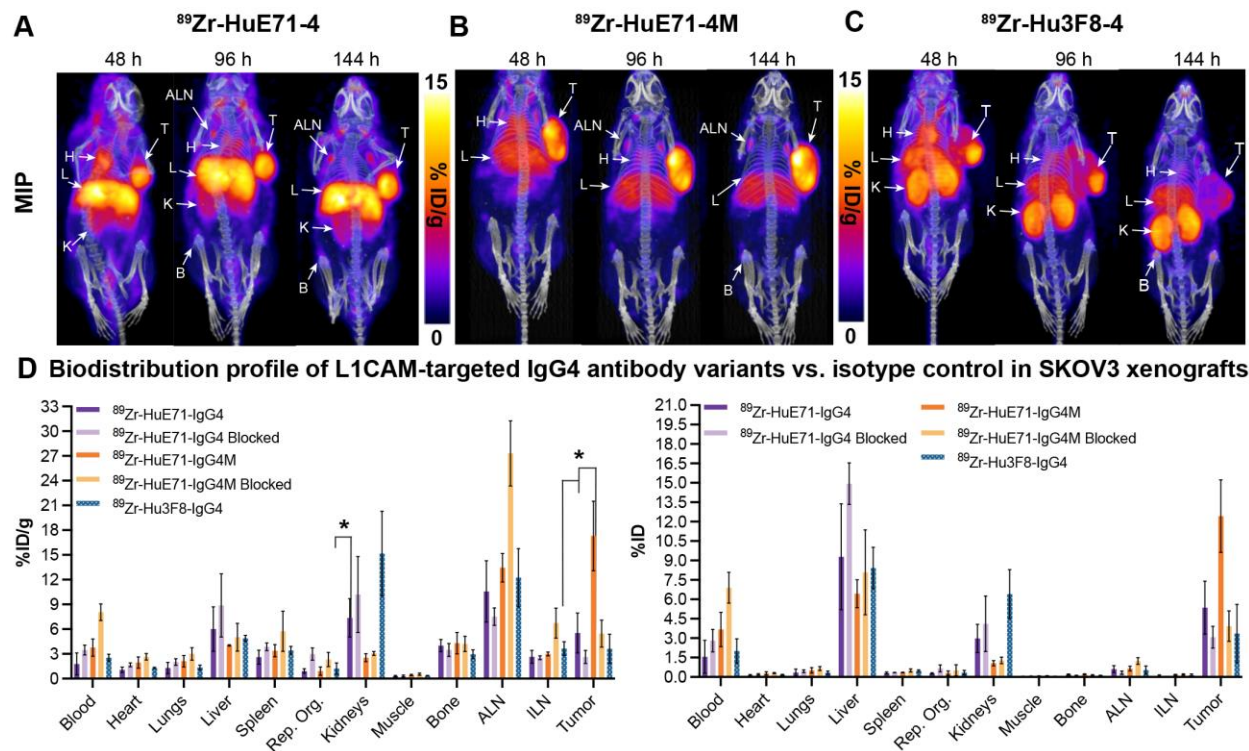


FIGURE 3. Immuno-PET imaging and ex vivo biodistribution analysis delineate the differential in vivo profiles of L1CAM-targeted IgG4 variants in SKOV3 xenografted mice. Longitudinal PET-CT images acquired at 48, 96 and 144 h p.i. of 1.8 mg/kg; 7.95 MBq; 45 μg of (A) ^{89}Zr -HuE71-IgG4; (B) ^{89}Zr -HuE71-IgG4M and (C) ^{89}Zr -Hu3F8-IgG4 – showing distribution of radioactivity in the blood (indicated by the heart – H), tumor (T), liver (L), kidneys (K) axillary lymph nodes (ALN) and long bone joints (B). Maximum intensity projections (MIPs) were calibrated and scaled 0-15% ID/g. (D) Ex vivo biodistribution profile (%ID/g vs. %ID) at 144 h p.i. of 0.25 mg/kg (1.15 MBq; 6.4 μg) of the two ^{89}Zr -labeled L1CAM-targeted IgG4 variants and the isotype control IgG4 Ab in SKOV3 xenografted mice. On the graph ILN = inguinal lymph node; * represents p value ≤ 0.05 . Detailed % ID/g and %ID values can be found in [Supplemental Tables 3 and 4](#).

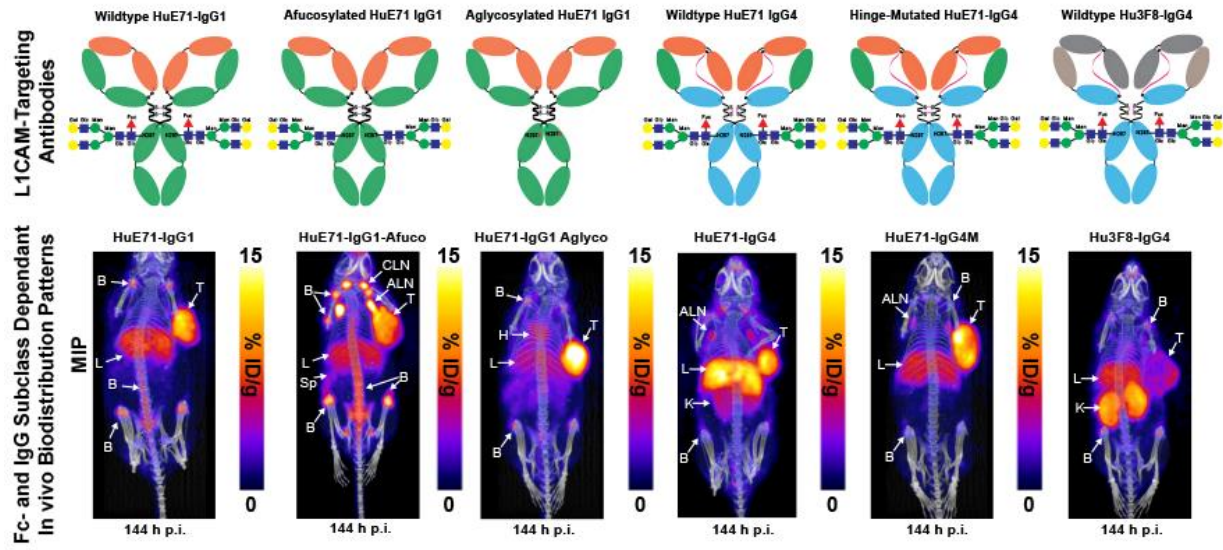
TABLE 1. Antibodies used in this study and their biochemical and functional characteristics.

Antibody	HuE71-IgG1	HuE71-IgG1 Afuco	HuE71-IgG1 Aglyco	HuE71-IgG4	HuE71-IgG4M	Hu3F8-IgG4
Target	L1CAM	L1CAM	L1CAM	L1CAM	L1CAM	GD2
Immunoreactive Fraction (%)	93.1 ± 2.2	89.5 ± 1.5	85.8 ± 2.9	86.7 ± 0.2	88.6 ± 0.3	NA
Subclass	IgG1	IgG1	IgG1	IgG4	IgG4	IgG4
Ab Modification	Wildtype IgG1	Afucosylated IgG1	Aglycosylated IgG1	Wildtype IgG4	S228P Mut IgG4	Wildtype IgG4
Fcγ R Binding	++	+++	-	+	+	+
Fab Arm Exchange	-	-	-	+	-	+

TABLE 2. Analysis of Fc-FcR binding by Surface Plasmon Resonance (Biacore T200)

Antibody	KD (M) mFcRIV	Relative mFcRIV Binding	KD (M) hFcRIIIa-158V	Relative hFcRIIIa-158V Binding
HuE71-IgG1	7.24E-07	1.00	8.73E-07	1.00
DFO-HuE71-IgG1	5.39E-07	1.34	6.64E-07	1.31
HuE71-IgG1-Afuco	2.27E-07	3.19	2.86E-07	3.05
DFO-HuE71-IgG1-Afuco	2.19E-07	3.31	2.94E-07	2.96
HuE71-IgG1-Aglyco	NB	-	NB	-
DFO-HuE71-IgG1-Aglyco	NB	-	NB	-

GRAPHICAL ABSTRACT



EXPERIMENTAL PROCEDURES:

Cell Culture

SKOV3 cells were purchased from the American Type Cell Culture (ATCC) in 2018. The cells were cultured in RPMI McCoy's 5A Medium, modified to contain 1.5 mM L-glutamine, 100 units/mL penicillin G and 100 µg/mL streptomycin and 10% fetal bovine serum. The cells were maintained at 37 °C in water-jacketed incubators and supplied with 5% CO₂. The cell lines were sub-cultured by splitting a T-150 flask (1:5) once per week using 0.25% trypsin/0.53 mM EDTA in Hank's Buffered Salt Solution without calcium and magnesium. In addition to routine testing for mycoplasma, SKOV3 cells were authenticated by STR profiling.

Construction and Expression of Different IgG Variants of the L1CAM-Targeting huE71

Antibody

Anti-human L1CAM monoclonal antibody E71 was developed in Dr Nai-Kong Cheung's lab in MSK and was humanized as detailed in patent application WO2018232188A1. Based on human homologs, CDR sequences of both heavy and light chains of E71 were grafted onto the human IgG1 framework. The combination of H1 and L1 sequences were chosen for production of the version of huE71 used in the current study. The huE71 genes (either wildtype or Fc-modified) were synthesized (Genscript, Piscataway, NY) and incorporated into a mammalian expression vector (Eureka, CA), and transfected into CHO-S cells for stable production. Similarly, human V_H and V_L sequences were fused to human IgG4 constant region (either wildtype or Fc-modified) to produce the IgG4 variants. Lastly, huE71-IgG1 genes were transfected into GnT1^{-/-} CHO cells to produce afucosylated huE71-1 IgG1.

HuE71 producer lines were cultured in OptiCHO serum free medium (Invitrogen, Carlsbad, CA) or PowerCHO-2 (Lonza, Basel, Switzerland) and the mature supernatant was harvested.

Protein A affinity column was pre-equilibrated with 25 mM sodium citrate buffer with 0.15 M NaCl, pH 8.2. Bound huE71 antibody variants were eluted with 0.1 M citric acid/sodium citrate buffer, pH 3.9 and alkalized (1:10 v/v ratio) in 25 mM sodium citrate, pH 8.5. The resulting eluant was passed through a Sartobind-Q membrane and concentrated to 5-10 mg/mL in 25 mM sodium citrate, 0.15 M NaCl, pH 8.2, and frozen in aliquots at -80°C.

Size Exclusion-High Performance Liquid Chromatography (SE-HPLC)

The purity of the antibodies was evaluated by size-exclusion high-performance liquid chromatography (SEC-HPLC). Sample purity and protein aggregation was analyzed using a TOSOH TSK-GEL G3000SWXL (7.8mm ID × 30cm) stainless column and TOSOH TSK-GEL SWXL (6.0mm ID × 4.0cm) guard column on a HPLC system (Shimadzu Scientific Instruments, Inc.). The eluant used was 0.4 M NaClO₄, 0.05 M NaHPO₄, pH 6.0. The flow rate was set at 0.5 ml/min and the run time was 40 min. Samples were passed through a 0.22µM filter (Millipore) prior to loading. The area under the curve by OD₂₈₀ was calculated for each protein peak in the HPLC chromatogram. The monomer peak consisted of proteins with MW of 150 kD. The salt peak was excluded from the AUC analysis.

Surface Plasmon Resonance

An SPR assay was set up on the Biacore T200 instrument (GE Healthcare) to determine the Fc-FcγR binding affinities (K_D) for the three L1CAM-binding IgG1 variants. To this end, recombinant mouse FcγRIV (1974-CD-050; R&D Systems) and human FcγRIII-158V isoform were employed as the ligand(s) whilst the L1CAM IgG1 variants were used as the analyte in the assay. The ligands were immobilized on a series S sensor chip CM5 (29401988; GE Healthcare) using an amine coupling kit (BR-1000-50; GE Healthcare) according to the standard procedure prescribed by the application wizard on the Biacore T200. High performance injections of the three

L1CAM IgG1 variants (42–667 nmol/L) were analyzed under the following conditions – 1 minute for association, 3 minutes for dissociation – both performed at a flow rate of 30 μ L/min. At the end of each cycle, the chip surface was regenerated using a 60s injection of 10 mM NaOH at a flow rate of 50 μ L/min. The kinetic data was analyzed using the Biacore T200 evaluation software. The data was fitted using a two-state reaction model: $A+B = AB = AB^*$, $K_D = (k_{d1}/k_{a1})/(1 + k_{a2}/k_{d2})$.

Antibody Conjugation

The various antibodies used in this study were buffer-exchanged from a solution of 25 mM sodium citrate and 150 mM sodium chloride to chelex-treated phosphate-buffered saline (PBS) by using separate PD-10 desalting columns (17085101, Cytiva Life Sciences) for each variant. The PD-10 columns were pre-equilibrated with chelex-treated PBS pH 7.2 (dead volume of 2.5 mL, elution volume of 2mL). Thereafter, the buffer-exchanged antibodies were concentrated to 2.5 – 4.0 mg/mL using Ultra-2 Amicon 50 kDa molecular weight cutoff (MWCO) filtration spin columns (UFC205024, Millipore). Thereafter, subject to the inventory available for each antibody, 1.2 – 3 mg (at concentrations > 2 mg/mL) of the antibody was aliquoted, and the pH of the antibody solution was adjusted to 8.7-9.0 using 1 M sodium carbonate (Na_2CO_3) prior to the gradual drop-wise addition of 10 molar equivalents of isothiocynato-desferrioxamine (*p*-SCN-Phe-DFO) (B-705; Macrocyclics, Inc.) dissolved in DMSO (41640; Sigma Aldrich) at a concentration of 10 mg/mL in DMSO. Care was taken to ensure that the volume of DMSO in the conjugation reaction mixture was <2% (v/v). The reaction mixture was incubated at 37 degrees Celsius ($^{\circ}\text{C}$) for 1 h with constant shaking at 500 rpm in a thermomixer. Thereafter, the antibody-DFO conjugates were purified from excess unconjugated DFO using separate PD-10 desalting columns (17085101, Cytiva Life Sciences) for each variant. The antibody-DFO conjugates collected in the 2 mL elution

fraction were subsequently concentrated to 3-5 mg/mL using Ultra-2 Amicon 50 kDa molecular weight cutoff (MWCO) filtration spin columns (UFC205024, Millipore).

⁸⁹Zr-radiolabeling

High specific activity zirconium-89 (⁸⁹Zr-oxalate) was procured from 3D Imaging (Little Rock, AR, USA). ⁸⁹Zr[Zr]-oxalate was neutralized using 1M sodium carbonate and ⁸⁹Zr-radioimmunoconjugates were prepared by mixing 44.4 MBq; 1.2 mCi of pH-adjusted ⁸⁹Zr[Zr]⁴⁺ with 200 µg of each of the DFO-conjugated antibodies suspended in chelex-treated PBS; pH 7.2. The mixture was incubated with gentle stirring for 1 h at 25 °C in a reaction volume of 300 µL to achieve a radioactivity concentration of 3.6 µCi/µL. The reaction progress was assayed via radio-thin layer chromatography (radio-TLC) on an AR-2000 Bioscan using silica-impregnated paper (ITLC-SG, Varian) with an eluent of 50 mM EDTA; pH 5. After 1 h, the radiolabeling reaction was quenched by adding 1/10 (v/v) 10 mM EDTA. Finally, the radioimmunoconjugates were purified promptly using a PD-10 desalting column for size-exclusion chromatography equilibrated with chelex-treated PBS (dead volume 2.5 mL and elution volume 2 mL). The purity of the radioimmunoconjugate preparation was assayed by radio-instant thin layer chromatography (radio-ITLC).

Radioimmunoconjugate Stability

The purified radioimmunoconjugates were tested for antibody stability and demetallation of ⁸⁹Zr⁴⁺ by incubating them in human AB-type serum for 6 days at 37 °C and the radiochemical purity was assayed via radio-TLC. Aliquots of each ⁸⁹Zr-antibody complex (100 µL) were incubated with 900 µL of human AB type serum and agitated constantly on a thermomixer at 37 °C. Samples were taken from each microcentrifuge tube and analyzed using radio-ITLC at day 0, 1, 3, 5, and 7 in triplicate. The stability of the complexes was measured as the percentage of

radioactivity that was retained at the origin of the radio-ITLC strip. This percentage was reported as % intact.

To investigate the integrity and stability of the various radioimmunoconjugates, SE-HPLC analysis was performed between incubation of the radioimmunoconjugate samples in chelexed PBS (no radioprotectant) and maintained at 37 °C with constant shaking at 400 rpm up to 6 days post-radiosynthesis. For SE-HPLC, a Phenomenex Yarra 3 µm SEC-3000 (300 x 7.8 mm) column was used on an HPLC system (Shimadzu Scientific Instruments, Inc.). The mobile phase used was an aqueous solution containing 100 mM sodium citrate tribasic dihydrate, 100 mM sodium chloride, pH 6.4. The flow rate was set to 1 mL/min and the run time was 20 minutes. Peaks on the 280 nm chromatogram were integrated using LabSolutions Postrun software (Shimadzu Scientific Instruments, Inc.).

Immunoreactivity

The immunoreactive fraction of the ⁸⁹Zr-DFO-antibodies was determined using a cell binding assay following procedures derived from Lindmo *et al* (1). To this end, SKOV3 cells were suspended in microcentrifuge tubes at concentrations ranging from 5.0 x 10⁵ – 5.0 x 10⁶ cells/mL in 500 µL PBS, 1% BSA (pH 7.4). Aliquots of ⁸⁹Zr-DFO-antibody (50 µL of 1 µCi/mL stock) were added to each tube to a final volume of 500 µL. The samples were incubated for 60 min on a thermomixer set to 37 °C and 500 rpm. The treated cells were pelleted by centrifugation (1400 rpm for 4 min), the supernatant was aspirated out and the pellet was washed three times with ice-cold PBS before removing the supernatant and counting the radioactivity associated with the cell pellets. The activity data were background-corrected and compared with the total number of counts

in appropriate control samples. Immunoreactive fractions were determined by linear regression analysis of total/bound radioactivity plotted against the inverse of normalized cell concentration.

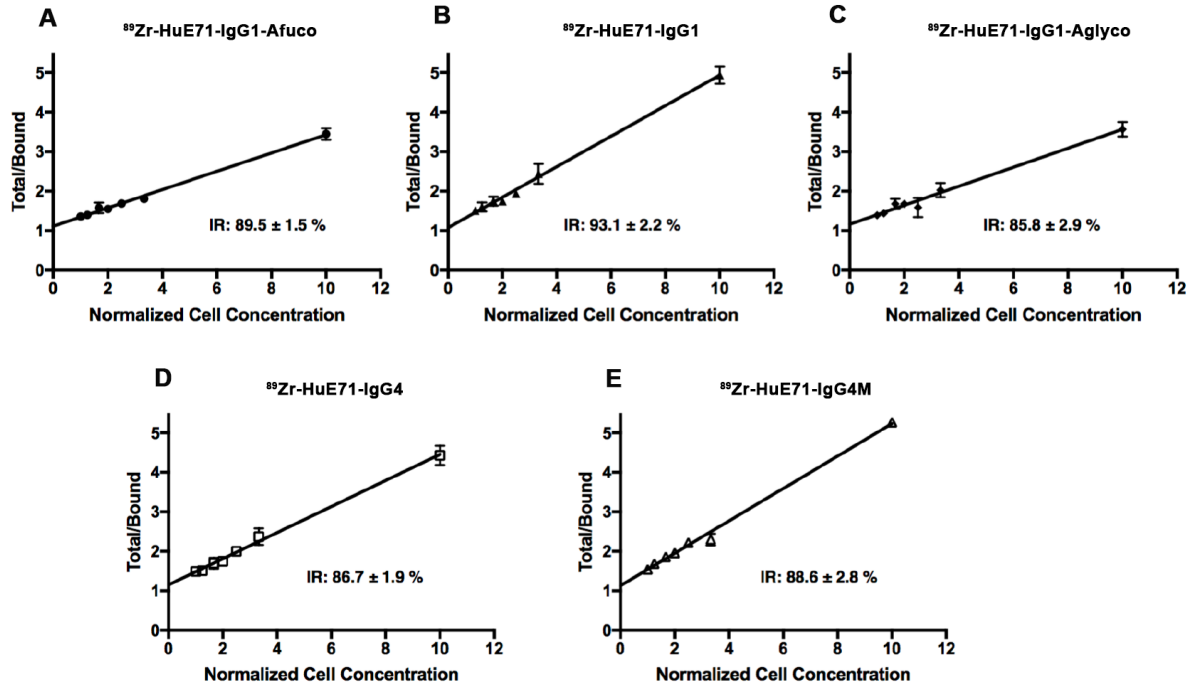
PET-CT Imaging

An energy window of 350-700 keV and a coincidence timing window of 6 ns were used for PET imaging. Acquired data was sorted into 2D histograms by Fourier rebinning, and transverse images were reconstructed by filtered back-projection (FBP) into a $128 \times 128 \times 63$ ($0.72 \times 0.72 \times 1.3$ mm³) matrix. The counting rates in the reconstructed images were converted to activity concentrations (percentage injected dose per gram of tissue, %ID/g) by use of a system calibration factor derived from the imaging of a mouse-sized water-equivalent phantom containing [⁸⁹Zr]Zr.

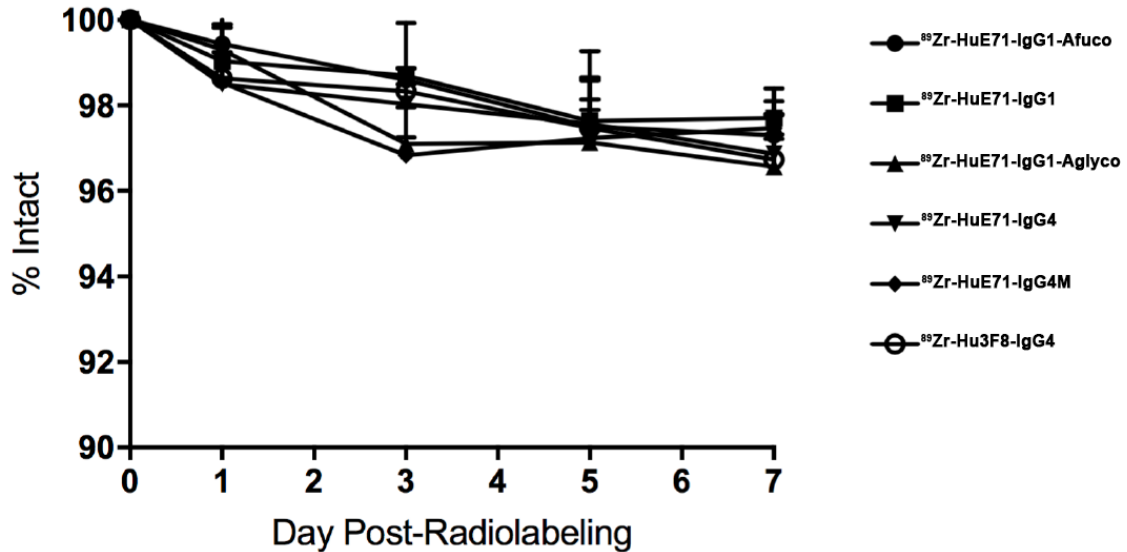
Histopathology

Tissue samples were fixed in 10% neutral buffered formalin and processed for histology. Paraffin embedded blocks were sliced to obtain 5µm sections and slides were stained with hematoxylin and eosin. Histopathologic analysis was performed in a blinded manner by a board-certified veterinary pathologist (AP).

SUPPLEMENTARY FIGURES

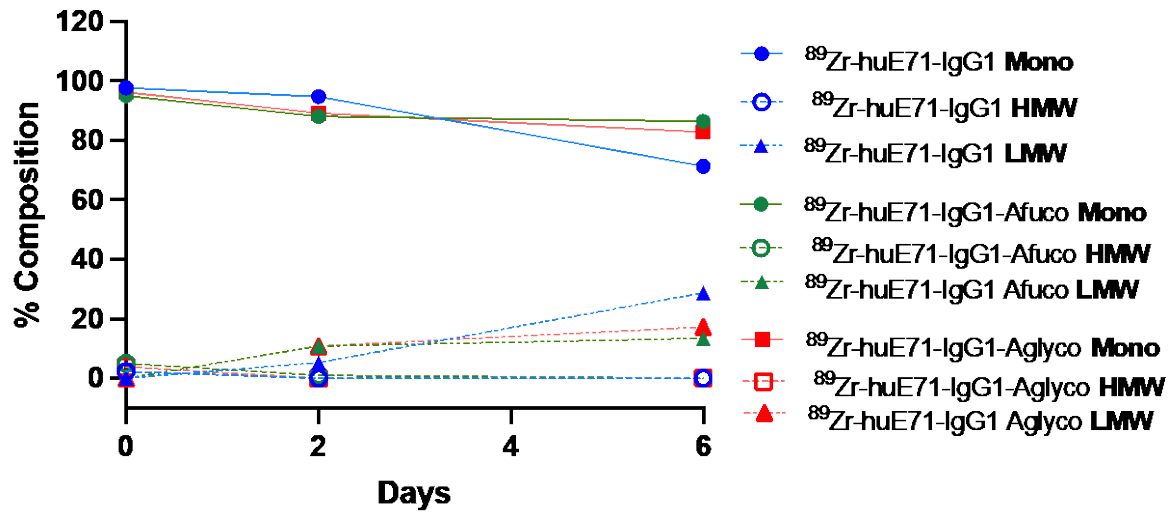


Supplemental Figure 1. Comparable immunoreactive fractions of the ⁸⁹Zr-labeled L1CAM IgG1 Fc-modified antibodies and IgG4 hinge variants.



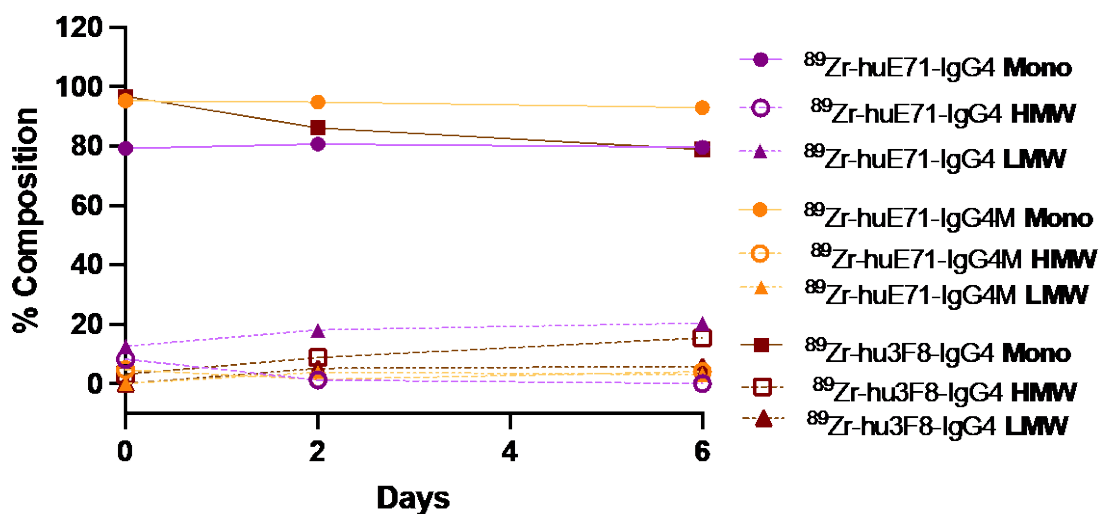
Supplemental Figure 2. Comparable in vitro serum stability of ⁸⁹Zr-labeled L1CAM antibody variants and isotype control ⁸⁹Zr-hu3F8-IgG4.

SE-HPLC Analysis: Stability of aL1CAM hlgG1 Fc-variants

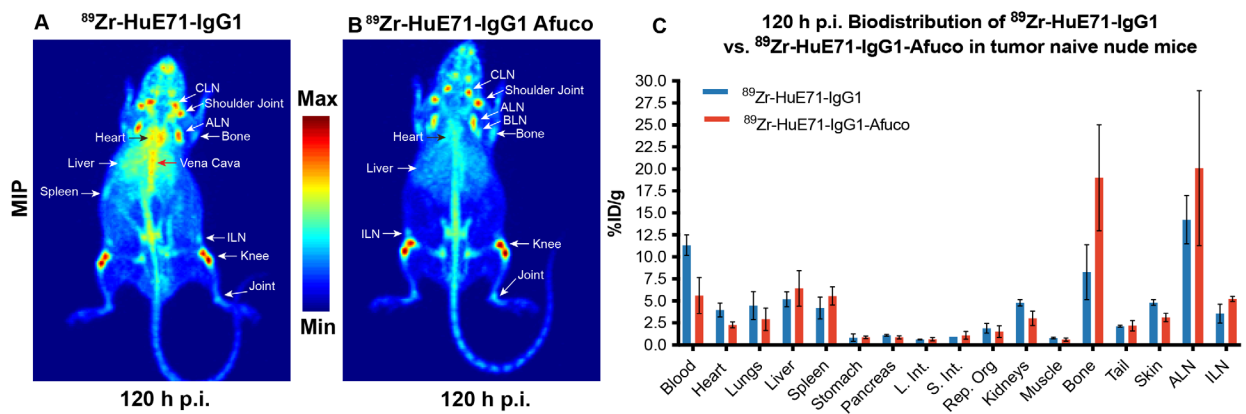


Supplemental Figure 3. SE-HPLC analysis demonstrating stability and integrity of the various anti-L1CAM ^{89}Zr -labeled Fc-modified IgG variants. Upwards of 80% of the IgG1 Fc-modified radioimmunoconjugates were found to be monomeric out to 6 days post-radiosynthesis. A gradual increase in two low molecular weight peaks was identified on the SE-HPLC chromatogram between day 2-6 of incubation in PBS without the presence of a radioprotectant in the solution.

SEC-HPLC Analysis: Stability of aL1CAM-hlgG4-variants



Supplemental Figure 4. SE-HPLC analysis demonstrating stability and integrity of the various anti-L1CAM ⁸⁹Zr-labeled IgG4 variants. Upwards of 75% of the IgG4 radioimmunoconjugates were found to be monomeric out to 6 days post-radiosynthesis. HuE71-IgG4 was found to have a relatively high percentage of low molecular weight (LMW) fraction from day 0. On the other hand, Hu3F8-IgG4 was found to have a relatively high percentage of high molecular weight (HMW) fraction in it. Nevertheless, the presence of LMW and HMW protein was <20%. The hinge mutated anti-L1CAM IgG4 Ab was found to have the best monomeric profile up to 6 days post-radiosynthesis.



Supplemental Figure 5. Immuno-PET imaging and ex vivo biodistribution analysis of L1CAM-targeted IgG1 variants in tumor naïve athymic nude (Nu/Nu) mice. PET-CT images acquired at 120 hours after intravenous injection of 1.8 mg/kg; 7.95 MBq; 45 µg of (A) ⁸⁹Zr-HuE71-1 – the wildtype IgG1 antibody – showing persistence of radioactivity in the heart, vena cava and jugular veins. High radioactivity concentrations were seen in the liver, joints of the long bones, pelvic bones and vertebrae. Uptake of radioactivity was also seen in the axillary, cervical and inguinal lymph nodes (ALN, CLN and ILN) – most likely owing to the high proportion of ⁸⁹Zr-HuE71-IgG1 remaining in systemic circulation due to the lack of a target sink (L1CAM-expressing tumor); (B) ⁸⁹Zr-HuE71-IgG1-Afuco – the ADCC-enhanced IgG1 variant – showing relatively less radioactivity persisting in systemic circulation (heart, vena cava and jugular veins). Relatively

low radioactivity concentrations are apparent in the liver, however, the joints of the long bones, pelvic bones and vertebrae showed high uptake of radioactivity. Radioactivity was also seen in the axillary, cervical and inguinal lymph nodes (ALN, CLN and ILN) – plausibly owing to a combination of ^{89}Zr -HuE71-IgG1-Afuco remaining in systemic circulation as well as Fc-Fc γ R interactions for this IgG1 variant; (C) Ex vivo biodistribution profile at 120 h after intravenous injection of 0.25 mg/kg (1.15 MBq; 6.4 μg) of the two ^{89}Zr -labeled L1CAM-targeted IgG1 variants in tumor naïve nude mice. Comparable uptake was found in most tissues except lower radioactivity concentration was found persisting in the blood and heart of tumor-naïve mice injected with ^{89}Zr -HuE71-1 MAGE but slightly higher uptake of radioactivity in the bones was found for this variant.

Supplemental Table 1 Comparative ex vivo biodistribution data (radioactivity concentrations) for the various ⁸⁹Zr-labeled L1CAM-targeted IgG1 antibody variants dosed in SKOV3 xenografts.

The values represent average ± standard deviation (n=3 animals per group).

Conjugate Tissues	⁸⁹ Zr-HuE71-IgG1 (% ID/g)	⁸⁹ Zr-HuE71-IgG1 Blocked (% ID/g)	⁸⁹ Zr-HuE71-IgG1-Afuco (% ID/g)	⁸⁹ Zr-HuE71-IgG1-Afuco Blocked (% ID/g)	⁸⁹ Zr-HuE71-IgG1-Aglyco (% ID/g)	⁸⁹ Zr-HuE71-IgG1-Aglyco Blocked (% ID/g)
Blood	5.2 ± 0.66	6.6 ± 0.66	0.8 ± 0.40	2.9 ± 0.14	3.7 ± 0.37	6.2 ± 0.07
Heart	2.0 ± 0.19	2.6 ± 0.53	0.7 ± 0.20	1.9 ± 0.20	1.7 ± 0.03	2.7 ± 0.21
Lungs	2.2 ± 0.05	2.9 ± 1.37	0.6 ± 0.20	1.4 ± 0.04	1.7 ± 0.14	2.9 ± 0.16
Liver	3.9 ± 1.78	3.8 ± 0.71	10.8 ± 2.10	7.2 ± 1.64	4.6 ± 1.42	4.4 ± 1.07
Spleen	3.5 ± 0.48	5.1 ± 0.25	3.5 ± 0.60	7.7 ± 0.60	3.3 ± 0.19	6.1 ± 1.48
Stomach	0.7 ± 0.14	0.8 ± 0.21	0.2 ± 0.10	0.2 ± 0.11	0.4 ± 0.08	0.5 ± 0.13
Pancreas	0.8 ± 0.21	0.8 ± 0.08	0.3 ± 0.10	0.4 ± 0.06	0.4 ± 0.09	0.6 ± 0.15
L. Intestine	0.7 ± 0.12	0.6 ± 0.23	0.2 ± 0.10	0.3 ± 0.08	0.4 ± 0.10	0.5 ± 0.04
S. Intestine	0.7 ± 0.06	0.9 ± 0.25	0.2 ± 0.10	0.4 ± 0.05	0.5 ± 0.13	0.7 ± 0.05
Rep. Organs	1.9 ± 0.53	2.0 ± 0.40	0.8 ± 0.20	1.0 ± 0.16	1.4 ± 0.66	1.9 ± 0.75
Kidneys	3.2 ± 0.44	3.3 ± 0.35	1.9 ± 0.60	2.6 ± 0.29	2.5 ± 0.28	3.3 ± 0.18
Muscle	0.5 ± 0.10	0.6 ± 0.04	0.3 ± 0.10	0.3 ± 0.07	0.4 ± 0.07	0.5 ± 0.08
Bone	8.3 ± 2.35	8.3 ± 1.81	6.6 ± 2.60	8.6 ± 1.66	3.7 ± 0.75	3.9 ± 1.65
Tail	1.3 ± 0.21	1.5 ± 0.33	1.0 ± 0.30	1.4 ± 0.44	0.7 ± 0.11	1.1 ± 0.26
Skin	2.8 ± 0.18	2.9 ± 0.64	1.9 ± 0.30	3.9 ± 1.23	2.0 ± 0.85	3.5 ± 0.23
ALN	14.1 ± 2.80	24.8 ± 6.36	25.5 ± 10.00	32.7 ± 2.95	6.1 ± 1.18	10.5 ± 1.89
ILN	3.2 ± 1.08	4.8 ± 0.81	4.2 ± 2.60	6.6 ± 1.39	2.4 ± 0.57	3.9 ± 1.33
Tumor	20.9 ± 2.22	6.8 ± 0.15	7.7 ± 2.00	3.0 ± 0.87	14.7 ± 4.53	4.9 ± 0.46

Supplemental Table 2. Comparative ex vivo biodistribution data (percentage of injected dose) for the various ⁸⁹Zr-labeled L1CAM-targeted IgG1 antibody variants dosed in SKOV3 xenografts. The values represent average ± standard deviation (n=3 animals per group).

Conjugate Tissues	⁸⁹ Zr-HuE71-IgG1 (% ID)	⁸⁹ Zr-HuE71-IgG1 Blocked (% ID)	⁸⁹ Zr-HuE71-IgG1-Afuco (% ID)	⁸⁹ Zr-HuE71-IgG1-Afuco Blocked (% ID)	⁸⁹ Zr-HuE71-IgG1-Aglyco (% ID)	⁸⁹ Zr-HuE71-IgG1-Aglyco Blocked (% ID)
Blood	4.8 ± 0.27	5.8 ± 0.65	0.7 ± 0.45	2.3 ± 0.52	3.9 ± 0.63	6.3 ± 0.03
Heart	0.3 ± 0.01	0.4 ± 0.06	0.1 ± 0.02	0.3 ± 0.04	0.3 ± 0.02	0.4 ± 0.11
Lungs	0.5 ± 0.05	0.5 ± 0.03	0.2 ± 0.05	0.3 ± 0.01	0.4 ± 0.06	0.6 ± 0.19
Liver	4.8 ± 0.35	5.4 ± 0.37	17.6 ± 3.39	11.3 ± 0.82	7.8 ± 2.56	7.7 ± 1.75
Spleen	0.4 ± 0.03	0.6 ± 0.06	0.4 ± 0.08	0.6 ± 0.15	0.3 ± 0.07	0.6 ± 0.11
Stomach	0.2 ± 0.04	0.3 ± 0.03	0.1 ± 0.04	0.2 ± 0.04	0.2 ± 0.05	0.3 ± 0.03
Pancreas	0.2 ± 0.00	0.3 ± 0.01	0.1 ± 0.02	0.1 ± 0.01	0.1 ± 0.03	0.2 ± 0.06
L. Intestine	1.0 ± 0.16	1.1 ± 0.07	0.4 ± 0.08	0.6 ± 0.10	0.9 ± 0.21	0.9 ± 0.01
S. Intestine	1.5 ± 0.21	1.8 ± 0.21	0.6 ± 0.13	0.9 ± 0.11	1.3 ± 0.10	1.7 ± 0.36
Rep. Organs	0.9 ± 0.11	0.6 ± 0.08	0.3 ± 0.05	0.3 ± 0.10	0.5 ± 0.29	0.6 ± 0.33
Kidneys	1.5 ± 0.07	1.5 ± 0.01	0.8 ± 0.23	1.0 ± 0.25	1.1 ± 0.06	1.5 ± 0.31
Muscle	0.1 ± 0.01	0.1 ± 0.01	0.04 ± 0.01	0.1 ± 0.01	0.1 ± 0.01	0.1 ± 0.02
Bone	0.3 ± 0.03	0.4 ± 1.05	0.2 ± 0.07	0.2 ± 0.07	0.2 ± 0.01	0.1 ± 0.02
Tail	0.9 ± 0.11	1.0 ± 0.29	0.6 ± 0.08	1.0 ± 0.31	0.6 ± 0.05	0.8 ± 0.26
Skin	0.1 ± 0.02	0.1 ± 0.05	0.1 ± 0.01	0.2 ± 0.05	0.1 ± 0.05	0.2 ± 0.03
ALN	0.7 ± 0.24	1.1 ± 0.03	1.3 ± 0.68	1.4 ± 0.29	0.4 ± 0.14	0.5 ± 0.13
ILN	0.1 ± 0.07	0.2 ± 0.05	0.2 ± 0.09	0.2 ± 0.07	0.1 ± 0.01	0.2 ± 0.05
Tumor	7.1 ± 1.52	1.7 ± 0.13	7.5 ± 2.47	2.4 ± 0.53	11.0 ± 2.90	4.5 ± 0.72

Supplemental Table 3. Comparative ex vivo biodistribution data (radioactivity concentrations) for the two ⁸⁹Zr-labeled L1CAM-targeted IgG4 antibody variants and the isotype control IgG4 antibody dosed in SKOV3 xenografts. The values represent average ± standard deviation (n=3 animals per group).

Conjugate Tissues	⁸⁹ Zr-HuE71-IgG4 (% ID/g)	⁸⁹ Zr-HuE71-IgG4 Blocked (% ID/g)	⁸⁹ Zr-HuE71-IgG4M (% ID/g)	⁸⁹ Zr-HuE71-IgG4M Blocked (% ID/g)	⁸⁹ Zr-Hu3F8-IgG4 (% ID/g)
Blood	1.8 ± 1.33	3.5 ± 0.59	3.8 ± 1.05	8.1 ± 1.00	2.5 ± 0.42
Heart	1.1 ± 0.33	1.7 ± 0.24	1.9 ± 0.69	2.6 ± 0.39	1.3 ± 0.09
Lungs	1.3 ± 0.68	2.0 ± 0.40	2.1 ± 0.70	3.0 ± 0.76	1.3 ± 0.30
Liver	6.0 ± 2.70	11.1 ± 0.06	4.0 ± 0.07	5.0 ± 1.69	4.9 ± 0.37
Spleen	2.6 ± 0.85	3.9 ± 0.46	3.4 ± 0.74	5.7 ± 2.44	3.4 ± 0.47
Stomach	0.2 ± 0.08	0.5 ± 0.23	0.3 ± 0.07	0.4 ± 0.01	0.2 ± 0.06
Pancreas	0.3 ± 0.11	0.5 ± 0.01	0.5 ± 0.10	0.5 ± 0.04	0.4 ± 0.01
L. Intestine	0.4 ± 0.06	0.7 ± 0.36	0.5 ± 0.13	0.6 ± 0.22	0.5 ± 0.05
S. Intestine	0.3 ± 0.07	0.4 ± 0.09	0.4 ± 0.11	0.6 ± 0.07	0.4 ± 0.07
Rep. Organs	0.9 ± 0.27	3.0 ± 0.76	0.9 ± 0.50	2.3 ± 0.86	1.2 ± 0.69
Kidneys	7.4 ± 2.32	10.2 ± 4.61	2.5 ± 0.48	3.1 ± 0.23	15.2 ± 5.14
Muscle	0.3 ± 0.08	0.3 ± 0.11	0.4 ± 0.07	0.5 ± 0.14	0.3 ± 0.03
Bone	4.0 ± 0.74	3.5 ± 0.78	4.3 ± 1.30	4.2 ± 0.92	3.0 ± 0.53
Tail	0.7 ± 0.16	0.8 ± 0.14	1.2 ± 0.38	1.1 ± 0.16	0.8 ± 0.17
Skin	1.5 ± 0.42	3.0 ± 0.68	2.3 ± 0.61	3.1 ± 1.03	2.1 ± 0.28
ALN	10.6 ± 3.72	7.5 ± 1.06	13.4 ± 1.73	27.3 ± 3.95	12.2 ± 3.53
ILN	2.7 ± 0.78	2.5 ± 0.22	3.0 ± 0.23	6.7 ± 1.82	3.6 ± 0.83
Tumor	4.4 ± 0.84	2.6 ± 0.79	17.3 ± 4.21	5.5 ± 1.64	3.6 ± 1.76

Supplemental Table 4. Comparative ex vivo biodistribution data (percentage injected dose) for the two ⁸⁹Zr-labeled L1CAM-targeted IgG4 antibody variants and the isotype control IgG4 antibody dosed in SKOV3 xenografts. The values represent average ± standard deviation (n=3 animals per group).

Conjugate Tissues	⁸⁹ Zr-HuE71-IgG4 (% ID/g)	⁸⁹ Zr-HuE71-IgG4 Blocked (% ID/g)	⁸⁹ Zr-HuE71-IgG4M (% ID/g)	⁸⁹ Zr-HuE71-IgG4M Blocked (% ID/g)	⁸⁹ Zr-Hu3F8-IgG4 (% ID/g)
Blood	1.6 ± 1.28	2.8 ± 0.86	3.7 ± 1.33	6.9 ± 1.19	2.0 ± 0.93
Heart	0.1 ± 0.06	0.2 ± 0.06	0.3 ± 0.12	0.3 ± 0.04	0.2 ± 0.03
Lungs	0.3 ± 0.27	0.5 ± 0.11	0.5 ± 0.21	0.7 ± 0.15	0.3 ± 0.12
Liver	9.3 ± 4.09	14.9 ± 1.61	6.4 ± 1.08	8.1 ± 3.27	8.4 ± 1.59
Spleen	0.3 ± 0.08	0.3 ± 0.02	0.3 ± 0.03	0.5 ± 0.12	0.5 ± 0.08
Stomach	0.2 ± 0.07	0.2 ± 0.04	0.2 ± 0.06	0.3 ± 0.05	0.3 ± 0.11
Pancreas	0.1 ± 0.02	0.1 ± 0.03	0.1 ± 0.02	0.1 ± 0.01	0.1 ± 0.01
L. Intestine	0.7 ± 0.21	1.0 ± 0.23	0.8 ± 0.09	1.1 ± 0.33	0.9 ± 0.08
S. Intestine	0.7 ± 0.23	1.0 ± 0.21	1.0 ± 0.27	1.4 ± 0.30	1.0 ± 0.17
Rep. Organs	0.3 ± 0.06	0.7 ± 0.27	0.3 ± 0.17	0.5 ± 0.43	0.3 ± 0.17
Kidneys	3.0 ± 1.1	4.1 ± 2.13	1.1 ± 0.20	1.3 ± 0.25	6.4 ± 1.89
Muscle	0.04 ± 0.01	0.1 ± 0.02	0.1 ± 0.02	0.1 ± 0.03	0.1 ± 0.01
Bone	0.2 ± 0.04	0.1 ± 0.02	0.2 ± 0.04	0.2 ± 0.02	0.1 ± 0.01
Tail	0.5 ± 0.13	0.5 ± 0.12	0.8 ± 0.25	0.7 ± 0.12	0.5 ± 0.07
Skin	0.1 ± 0.03	0.1 ± 0.03	0.1 ± 0.03	0.1 ± 0.03	0.1 ± 0.05
ALN	0.6 ± 0.26	0.3 ± 0.13	0.6 ± 0.18	1.2 ± 0.26	0.5 ± 0.3
ILN	0.1 ± 0.05	0.1 ± 0.002	0.2 ± 0.03	0.2 ± 0.05	0.1 ± 0.08
Tumor	5.4 ± 2.05	3.1 ± 0.84	12.4 ± 2.80	3.9 ± 1.18	3.4 ± 2.25

REFERENCES

- (1) Lindmo, T., Boven, E., Cuttitta, F., Fedorko, J., and Bunn, P. A., Jr. (1984) Determination of the immunoreactive fraction of radiolabeled monoclonal antibodies by linear extrapolation to binding at infinite antigen excess. *J Immunol Methods* 72, 77-89.